Aerospace Science and Technology 118 (2021) 106990

Contents lists available at ScienceDirect

Aerospace Science and Technology

www.elsevier.com/locate/aescte

Effects of wing kinematics, corrugation, and clap-and-fling on aerodynamic efficiency of a hovering insect-inspired flapping-wing micro air vehicle

Khanh Nguyen [a], Loan Thi Kim Au [b], Hoang-Vu Phan [a,1], Soo Hyung Park [c], Hoon Cheol Park [a,*]

[a] Department of Smart Vehicle Engineering, Konkuk University, Seoul, South Korea
[b] Department of Aerospace Engineering, Sejong University, Seoul, South Korea
[c] Department of Aerospace Information Engineering, Konkuk University, Seoul, South Korea

ARTICLE INFO

Article history:
Received 2 April 2021
Received in revised form 17 July 2021
Accepted 20 July 2021
Available online 2 August 2021
Communicated by Huihe Qiu

Keywords:
Aerodynamic efficiency
Corrugation
Clap-and-fling
Flapping-wing micro air vehicle
Biomimetics
Computational fluid dynamics

ABSTRACT

A flapping-wing micro air vehicle (FW-MAV) operating with aerodynamically optimal wing configuration and kinematics may save energy and thus prolong flight time. In this work, we use a computational-fluid-dynamic method to investigate the effects of wing kinematics, corrugation structures, and clap-and-fling on the aerodynamic efficiency of our hovering two-winged FW-MAV (KUBeetle). From the measured reference wing kinematics, we generated several different wing kinematics, considering the effect of spanwise twist and chordwise camber that produce high lift-to-drag ratio (L/D). Among the investigated cases, the modified wing kinematics version 3, which includes both camber and twist with an average angle of attack of about 37°, was selected, because of its ~24% improvement of L/D, while maintaining similar lift to the measured reference wing kinematics. The results also showed that the camber plays a role in the improvement of both lift and L/D, which improvements are approximately (16.7 and 10.6)%, respectively. We then used wing kinematics version 3 to investigate the effects of various leading-edge corrugation structures. Based on the results of lift and L/D, we proposed a wing with distributed wing corrugations along the wingspan, which slightly augments the L/D by 2%. In addition, to see how the clap-and-fling behavior contributes to the aerodynamic efficiency, its effects on lift and drag generation were examined. We found that the clap-and-fling enhanced lift by 5%, but increased drag by 9%, resulting in a 4% reduction of the L/D for both the measured and the modified wing kinematics. Thus, the lift-augmented clap-and-fling is inefficient for FW-MAVs. Finally, the study confirmed that the wing with distributed wing corrugations using wing kinematics version 3 without clap-and-fling presented at the stroke reversals is preferable for the high aerodynamic efficiency of the KUBeetle robot, with 31% improvement in L/D.

1. Introduction

Over the past few decades, flying insects have become a great source of inspiration for the development of flapping-wing micro air vehicles (FW-MAVs). Many studies of insect flight have therefore been conducted to understand their flight mechanisms [1–3]. These mechanisms include leading-edge vortex [4,5], wing–wake interaction or wake capture [6–8], wing rotation [9,10], clap-and-fling [11–16], wing flexibility [17–22], distribution of spanwise angle of attack (AoA) [23–25], and wing corrugation [19,26–31]. Thanks to those studies, several tailless FW-MAVs are ready for untethered flight; for example, Nano Hummingbird [32], KUBeetle [33], Colibri robot [34], Robobee [35], Delfly Nimble [36], NUS-Roboticbird [37], and Purdue hummingbird [38]. However, there are still limitations in flight time that require further improvements of the robots. Therefore, extensive optimizations of the wing configuration and kinematics have been considered. For example, wing flexibility including chordwise camber and spanwise twist was found beneficial for force generation and power requirement [19,21,39]. Okamoto et al. [19] experimentally compared a cambered wing and a thin flat plate and concluded that the curved wing with 9% chord height increased the maximum lift coefficient ($C_{l,max}$), minimum drag coefficient ($C_{d,min}$), and slope of aerody-

* Corresponding author.
E-mail address: hcpark@konkuk.ac.kr (H.C. Park).
[1] Current address: School of Engineering, Swiss Federal Institute of Technology Lausanne (EPFL), Lausanne, Switzerland.

https://doi.org/10.1016/j.ast.2021.106990
1270-9638/

namic efficiency (C_l/C_d) with respect to the AoA. Truong et al. [21] used unsteady blade element theory to numerically analyze the effect of wing twisting on lift enhancement in flapping wings and found that a flapping wing with a negative twist configuration produced about 10% more vertical force, while consuming less power than the flat wing. In addition, Sane et al. [23], Phan et al. [24], and Gehrke et al. [25] identified a range of spanwise AoAs to achieve low drag but high lift. Reference [25] experimentally optimized the pitch angle kinematics to maximize the cycle-average lift and aerodynamic efficiency. The kinematics with high AoA achieved the lowest average aerodynamic efficiency of $\eta = 0.6$, and the highest average lift coefficient of $C_l = 2.09$. Meanwhile, the relatively lower pitch angle kinematics increased the average aerodynamic efficiency by 93%, $\eta = 1.17$, but reduced the stroke average lift coefficient by 43% of its maximum value, resulting in $C_l = 1.20$ [25].

The corrugation of insect wings was investigated for both aerodynamic and structural purposes. Rees [26] compared the corrugated airfoil and smoothed envelop to investigate the contribution of wing corrugation to bending stiffness. His works inspired scientists to explore the potential use of corrugated wings in FW-MAVs. Vargas et al. [31] investigated the effect of two-dimensional (2D) corrugated dragonfly wings and showed that the aerodynamic efficiency or lift-to-drag ratio (L/D or C_l/C_d) was slightly improved, compared to that of its smooth counterpart. An experimental study of three-dimensional (3D) corrugated dragonfly wings showed a similar result [28]. However, Meng et al. [30], based on their calculations by computational fluid dynamics (CFD), concluded that the insignificance of the wing corrugation effect is due to the flow separation in the high AoA of (35 to 50)°. Au et al. [29] performed 3D CFD analysis for several corrugated wings, finding that when the same wing kinematics were applied for both smoothed and corrugated wings, the contribution of corrugation to aerodynamic efficiency was insignificant. A 2D CFD study by Dao et al. [27] indicated that the leading-edge corrugation placed at the upper and lower parts of the chord at 37.5% of the wing length (inboard wing with a relatively higher AoA), increased the L/D by about 8%, but that at 75% of its spanwise length (outboard wing with a relatively lower AoA), decreased the L/D by 2.4%, compared to that of the smooth profile.

The clap-and-fling effect, which has been extensively studied in insects [15,40–42], also serves as a lift-enhancing mechanism in FW-MAVs [16,36,43–45]. Zdunich et al. [45] built a four-wing Mentor flapping-wing robot and reported that the implemented clap-and-fling effect increased the lift by approximately 50%. Nguyen et al. [43] also revealed that the clap-and-fling effect increased the lift of their X-wing FW-MAV by about 45%. The clap-and-fling effect was successfully implemented in the two-wing KUBeetle robot, with a stroke amplitude of more than 180° [16]. The study showed that the clap-and-fling effect improved the vertical lift force by 16.2%, when compared to that without the effect.

As described above, most studies have focused on lift improvement, whereas only a few reports on the aerodynamic efficiency of actually flying insect-like tailless FW-MAVs have been made [36,46]. Interestingly, a breakdown of the power consumption of a flapping-wing system showed that about 48% of the total power was consumed to produce aerodynamic forces [47], while about 20% was consumed to overcome inertial force developed during the flapping wing motion. To reduce the inertial power consumption, the wing mass must be as light as possible. For example, the specially designed foldable wings in one report [48] are about 10% heavier than the lightweight wings used in another [46]. Therefore, the endurance of the robot with the lightweight wings [46], should be longer than that with the foldable wings [48]. Still, the major portion of the power is spent on producing aerodynamic forces. The improvement of aerodynamic efficiency is crucial to extending the endurance of a FW-MAV.

In this study, we performed a series of three-dimensional CFD analyses using ANASYS-Fluent to investigate the aerodynamic efficiency of the KUBeetle, a tailless insect-like FW-MAV, which uses the trailing-edge-change (TEC) mechanism to produce the control moments [21]. Based on the CFD simulation, a spanwise range of AoA was identified for high aerodynamic efficiency from the measured reference wing kinematics of the KUBeetle. Then, based on the finding, four higher performing wing kinematics were created. We modulated the wing kinematics by adjusting the spanwise AoA and chordwise camber, such that the physical nature of the measured flapping wings was maintained. The aerodynamic performance of each modified wing kinematics was evaluated and compared to that for the measured reference wing kinematics. In addition, the wing corrugation was studied for one of the suggested modified wing kinematics, which satisfied the requirement of lift. Subsequently, seven leading-edge corrugated wings were numerically tested to propose a wing model with a combined corrugation in the spanwise direction that showed higher aerodynamic efficiency at each of the five investigated spanwise locations. We also investigated the effect of wing corrugation on the aerodynamic efficiency of the flapping wings with the clap-and-fling effect.

2. Materials and methods

2.1. Wing kinematics of the KUBeetle

Similar to the previous works [49–51], we use the coordinate systems shown in Fig. 1 to describe the dynamic motion of the flapping wings, where $O_e x_e y_e z_e$ is the fixed coordinate system on the earth, while $O_b x_b y_b z_b$ is the coordinate system attached to the body. The wing pivot point at the origin O in the wing is the reference position used to identify the center of gravity ($CG \equiv O_b$). The x_b-axis points backward in the opposite direction to flight, while the y_b-axis points to the right wing. Meanwhile, the z_b-axis is aligned with the body axis, which points to the top. The coordinate system $Oxyz$ is used to determine the wing motion in hover (see Fig. 1b). At the local spanwise position, the wing camber is defined in terms of the middle and full rotation angles, denoted by θ_m and θ_f, respectively, as follows:

$$Camber(r) = \frac{h}{c} \times 100\% = \frac{1}{2}\tan\left(\theta_m - \theta_f\right) \times 100\%, \tag{1}$$

where h is the mid-chord height, and c is the full-chord length. The full rotation angle, θ_f, is the angle between the stroke plane and the full-chord line connecting the leading-edge and trailing edge. Meanwhile, the middle rotation angle, θ_m, is the angle between the stroke plane and the mid-chord line connecting the leading edge and the mid-chord point. The geometric AoA (α) is defined as the angle between the inflow and the full-chord, while ψ denotes the flapping angle between the feather axis and y-axis. The measured reference wing kinematics of the KUBeetle previously presented [21] were captured using three synchronized high-speed digital cameras and digitized using DLTdv tool [52].

Fig. 2a shows the nine markers on the wing, and the four others on the body frame, which we placed to measure the wing kinematics. The time histories for the flapping angle and rotational angles were calculated based on their coordinates captured over a flapping cycle. To reproduce the wing motion in the CFD simulation, the Fourier series function was used to fit the measured reference wing kinematics, as shown in Eq. (2):

$$f(t) = a_0 + \sum_{k=1}^{n=9} \left[a_k \cos(2k\pi f t) + b_k \sin(2k\pi f t)\right], \tag{2}$$

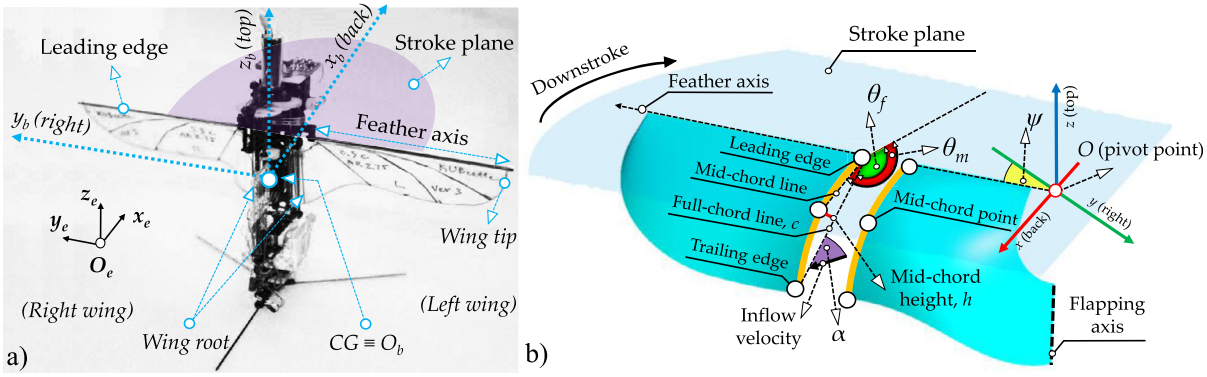

Fig. 1. Definition of coordinates and angles: a) For the KUBeetle robot, and b) for the wing motion.

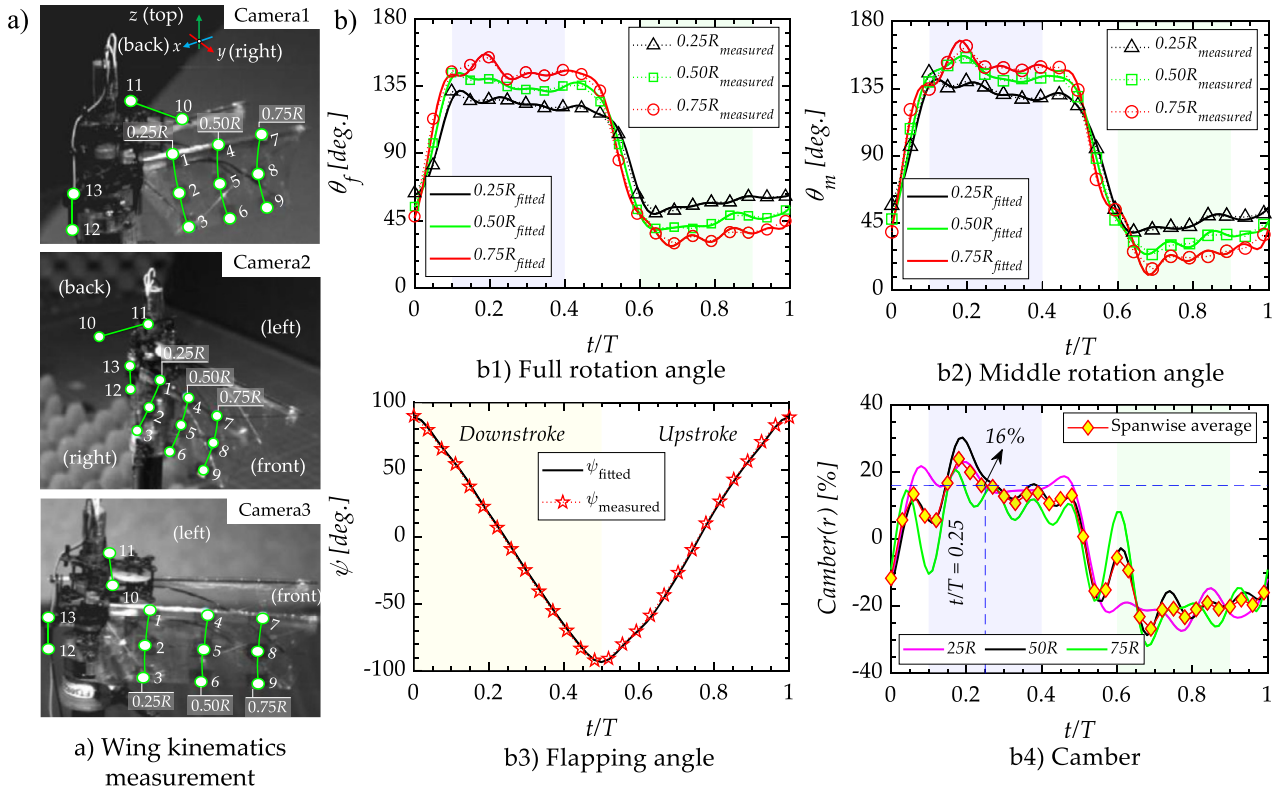

Fig. 2. The measured reference wing kinematics of the KUBeetle: a) Images with the enhanced markers captured by three high-speed cameras, b) measured and fitted wing kinematics at the three wing locations of (0.25, 0.5, and 0.75)R. (For interpretation of the colors in the figure(s), the reader is referred to the web version of this article.)

where the identified coefficients a_0, a_k, and b_k are designated in the user-defined-function (UDF) code in ANSYS-Fluent to describe the flapping motion. Fig. 2b presents the measured and fitted wing kinematics of the KUBeetle at (0.25, 0.5, and 0.75)R. Equation (1) is then used to calculate the wing cambers. The spanwise-average camber, denoted by the yellow diamond with solid red line, is considered as the reference for the wing kinematics modulation.

2.2. Computational fluid dynamics (CFD) modeling

The CFD model of flapping wings was created by following the same method described in [49], which could provide converged solutions with an acceptable accuracy, as validated elsewhere [16,49–51]. For the grid independency of the non-corrugated and corrugated wings, the present mesh for each case was constructed with similar grid resolution to that which was applied in the previous grid independency study [50]. Thus, we expect that the acquired results by the CFD are mesh independent. The spanwise length, R is referenced to construct the three-dimensional (3D) computational domain (Fig. 3a). Due to the symmetric flapping motion, only one wing is simulated. The domain is a 3D half-cylinder measuring $12R$ in length and $12R$ in diameter, which is filled by about 4.7 million tetrahedral elements. The domain is extended $6R$ forward to the inlet from the pivot point, and $6R$ upward to the top. The distance from the flapping axis to the symmetry plane is 8 mm. The mesh is finest surrounding the wing in the high-density region, occupying about 50% of the total elements. The maximum grid length in this high-density region is 2.0 mm, while the wing is modeled by about sixty thousand triangular elements, whose maximum element edge length is 0.4 mm, which is equivalent to 1.6% c_{max}, as shown in Figs. 3b. Thus, the mesh size becomes coarser toward the far field, and the inlet and outlet boundaries. Figs. 3b and c describe the unstructured meshes of the non-corrugated wing and a corrugated wing (see subsection

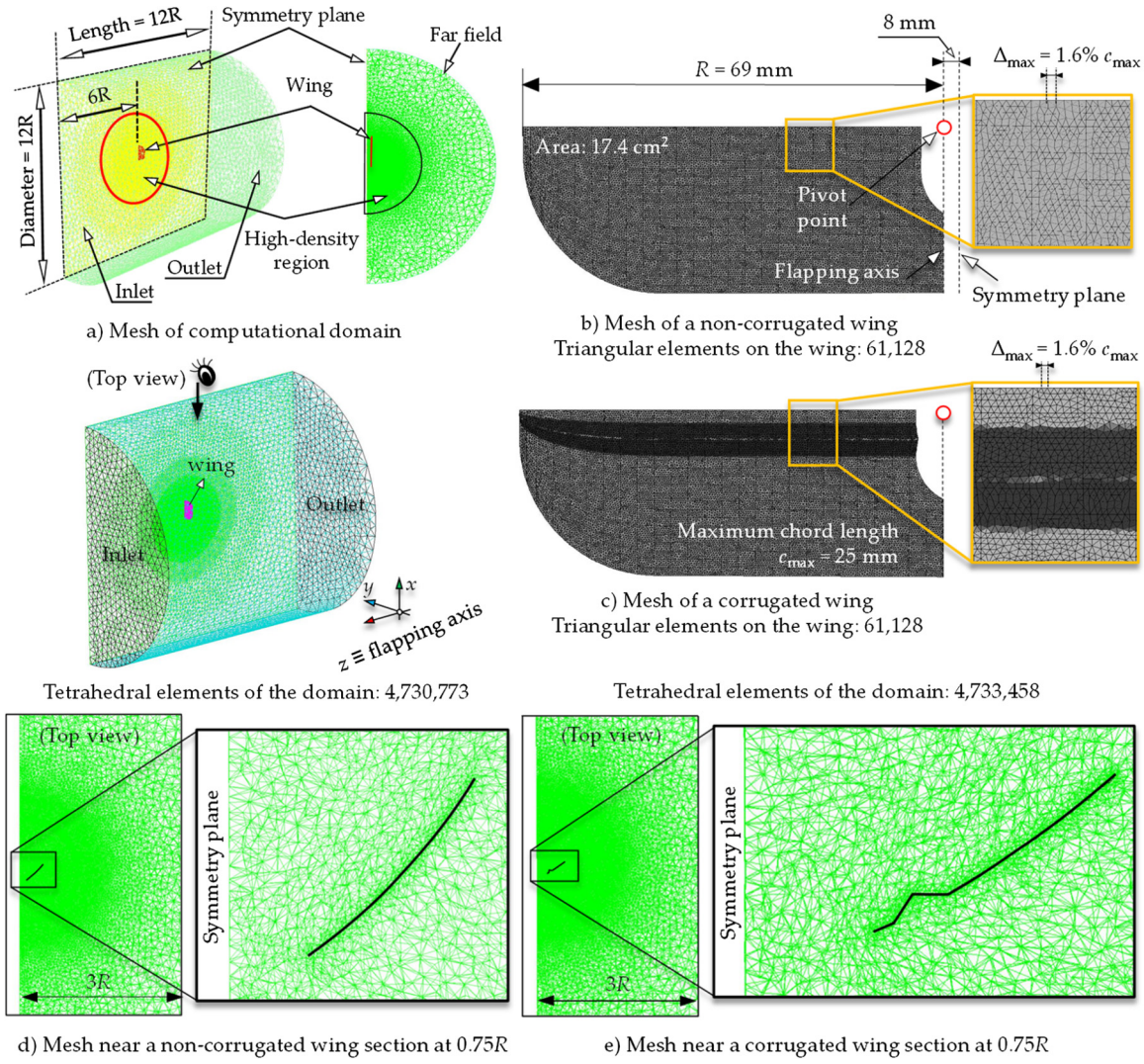

Fig. 3. CFD modeling: a) the computational domain, b) mesh of a non-corrugated wing, c) mesh of a corrugated wing, d) mesh near a non-corrugated wing, and e) a corrugated wing.

2.4), respectively, while Figs. 3d and e detail their mesh generations around the wing sections at $0.75R$, respectively. The number of triangular grid cells on the wing surface are 61,128 elements for both wings, as shown in Figs. 3b and c, while the computational domains of the two wings are modeled by about 4,734,000 tetrahedral elements for the two cases, as shown in Figs. 3d and e. The boundary layer thickness is about 4% $c_{\max}$ at $0.75R$, which can be calculated by the Blasius solution [53]. In the CFD models, the minimum distance between the wing surface and the first grid point is an order of 0.1% $c_{\max}$. Therefore, the current mesh near the wing surface is small enough to resolve laminar boundary layers. The time step is set to be 1/1,000th of the flapping cycle.

Equation (3) shows the definition of the local Reynolds number, Re [14] in a spanwise location of r:

$$Re(r) = \frac{u_{\text{mean}}(r) \times c(r)}{\nu} = \frac{2rf\Phi \times c(r)}{\nu}, \tag{3}$$

where r is the spanwise position, u_{mean} is the mean flapping velocity, $c(r)$ is the local chord length, f is the flapping frequency, Φ is the wingbeat amplitude (in rad), and ν is the kinematic viscosity of the air. The Re range from the root along the wing length of the TEC robot is about 10^3 to 10^4, as reported in [29]. This range is not small enough to consider the flow environment as a pure laminar regime. In particular, when we study flow structure after separation, the turbulent diffusion should be taken into account. Meanwhile, the laminar models provided trustworthy results for the flapping-wing calculations with less computing time, as reported elsewhere [29,49–51]. Lian et al. [54] numerically tested a flapping wing made of NACA0012 airfoil at chord Re numbers of 1.2×10^4, 2×10^4, and 4×10^4. In their simulation, they applied the laminar flow option, and found that the computed flow pattern was very close to the measurement. In addition, the power coefficients from their laminar flow simulation closely predicted the measurement. Young et al. [55] performed CFD analysis on a flapping dragonfly wing for Re numbers of 484 and 29,048 and compared the effects of laminar flow and the detached-eddy-simulation turbulence model on the force generation. They suggested that there were essentially no differences in aerodynamic forces computed by the laminar and turbulent flow options. This means that the evolution of turbulence does not contribute to meaningful change in the magnitude of force produced by flapping wings in the Re range of 10^4, even though turbulent flow may alter the flow structure after separation. Therefore, for the study of the KUBeetle, a CFD with the laminar flow option may reasonably predict the formation and separation of leading-edge vortex (LEV) and trailing-edge vortex (TEV) on the wing surface providing acceptable cycle-average forces.

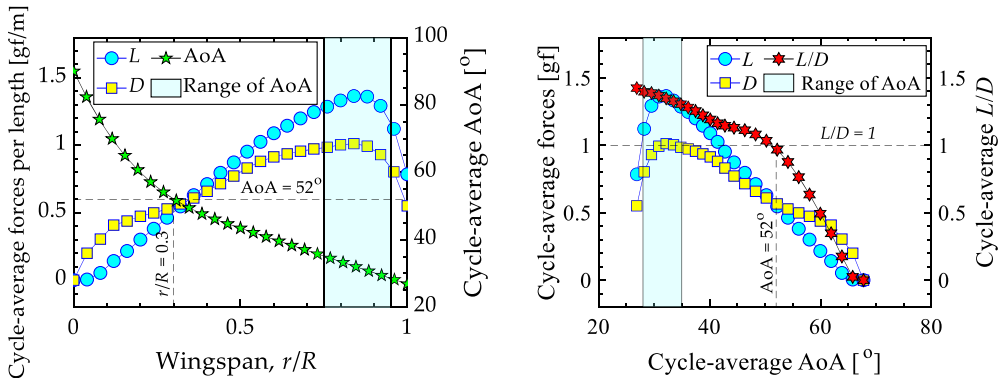

Fig. 4. Characteristics of the measured reference wing kinematics: a) Cycle-average forces per length and AoA over the wingspan, b) cycle-average forces and L/D with respective to the average AoAs (shaded area representing the suggested range of the AoAs).

2.3. Method of wing kinematics modulation

The measured wing kinematics of the KUBeetle, which used the TEC control mechanism, is considered as the reference wing kinematics. Thus, it is named the TEC-WK. The reference TEC-WK is modulated to improve the aerodynamic efficiency. In the modified wing kinematics, the flapping angle (ψ) is the same as that of the TEC-WK (Fig. 2b3). The implemental strategy to suggest a modified wing kinematics must ensure that all the physical natures of the flapping wings are maintained, which is described as follows. In the first step, the spanwise-average camber of the TEC-WK is calculated at each time (t/T) using Eq. (1). Then, the camber at each time of the modified wing kinematics, which is based on the spanwise-average camber of the TEC-WK computed at the same time, is assumed to be constant from wing root to tip. For example, the spanwise-average camber of the TEC-WK (Fig. 2b4) at $t/T = 0.25$ is about 16%. Then, the camber of the modified wing kinematics at each spanwise location at $t/T = 0.25$ is suggested based on this spanwise-average camber of the TEC-WK. However, the spanwise-average camber of the TEC-WK appears to not be perfectly symmetric between the downstroke and upstroke (Table 1). Hence, we create a symmetric camber between two half-strokes in the modified wing kinematics by proportionally modulating the TEC-WK's camber, such that the lift produced by each half-stroke is close to the other.

Second, Equation (4) expresses the geometric angle of attack (α or AoA). The AoAs of the TEC-WK providing relatively high aerodynamic efficiency, which are based on the simulation results, are used to adjust the AoAs of the modified wing kinematics:

$$\text{For downstroke: } \alpha = \pi - \theta_f \quad \text{and} \quad \text{for upstroke: } \alpha = \theta_f. \qquad (4)$$

In Fig. 4a, the left vertical axis indicates the cycle-average forces per length produced along the wingspan. The right vertical axis represents the cycle-average AoA over the spanwise location, which is interpolated based on the mean AoAs calculated at (0.25, 0.5, 0.75, and 1.0)R during the translational stages of the downstroke ($0.1 \leq t/T \leq 0.4$) and upstroke ($0.6 \leq t/T \leq 0.9$). Fig. 4b presents the cycle-average lift (L), drag (D), and L/D versus the cycle-average AoA. Note that the lift here is the force component in the vertical direction, while the drag is the horizontal force component of the resultant force. The shaded areas in the two plots stand for a range of AoA of (28–35)°, where the lift and aerodynamic efficiency are relatively high. This AoA range corresponds to the spanwise locations from (0.75 to 0.95)R (Fig. 4a), where a large portion of the aerodynamic force is generated in a wing. Another important note is that the L/D ratio at $\alpha \approx 52°$ is close to that at $0.3R$, and when $\alpha > 52°$, it becomes less than one. Therefore, the cycle-average AoA of the modified wing kinematics must stay within the recommended range (28–35)°.

As the third step, using Eqs. (1) and (4), the camber or middle rotation angle of the modified wing kinematics are created and presented in Figs. 5a–e, based on their suggested instantaneous AoAs and the spanwise-average camber of the TEC-WK. Finally, for the modified wing kinematics with wing twist, the wing twist ratios of the TEC-WK at each time, which are defined in this work as the ratio of the AoA of the two locations of (0.25 and 0.75)R to the AoA at $0.5R$, are proportionally modulated for the modified wing kinematics. However, this step ensures that the cycle-average AoA at $0.25R$ is less than 50°, and that at $0.75R$, it is in the range (28–35)°.

Based on the guidelines, Table 1 and Fig. 5 propose and present the four modified wing kinematics, which are named the wing kinematics ver1, ver2, ver3, and ver4. Table 1 shows the half-cycle-average AoAs and spanwise-average camber of the five wing kinematics. Note that the average calculation is taken during the translational stages, *e.g.*, t/T = (0.1 – 0.4) in the downstroke, and t/T = (0.6 – 0.9) in the upstroke. For the reference TEC-WK, the differences of the spanwise-average camber in the two half-strokes are relatively large, which implies that the camber of the TEC-WK is asymmetric. For example, the spanwise-average camber in the downstroke is 14.5%, while in the upstroke it is 19.5%. This explains why the lift is asymmetrically produced in the two half-strokes, *e.g.*, 9.4 gf in the downstroke, and 10.8 gf in the upstroke. Hence, the half-cycle-average camber of the TEC-WK is adjusted and applied in the modified wing kinematics to minimize the difference of lift produced by the two half-strokes of each modified wing kinematics. Figs. 5a–d present the four modified wing kinematics, including the middle and full rotation angles. Meanwhile, the flapping angle is identical to that of the TEC-WK (Fig. 2b3). Fig. 5e presents the spanwise-average cambers of the modified wing kinematics. They are modified to ensure that the forces generated by the two half-strokes are close to each other, and their spanwise-average cambers are close to that of the TEC-WK. For example, Table 2 shows that the spanwise-average camber of the wing kinematics ver3 during the translational stages is about 17.2%, which is similar to that of the TEC-WK, of about 17%. Fig. 5f plots the distributions of the cycle-average AoAs along the wingspan for the five wing kinematics. The cycle-average AoAs from $0.25R$ to the wing tip are similar, as can be seen in ver1 and ver2. Therefore, we define that the cases ver1 and ver2 are with chordwise camber, but without spanwise twist.

2.4. Wing corrugations

This section investigates the effect of the corrugated wings on the aerodynamic efficiency for the modified wing kinematics ver3, which satisfies the requirements of the force and aerodynamic efficiency. Based on the CFD analysis of the 2D flapping wings, a

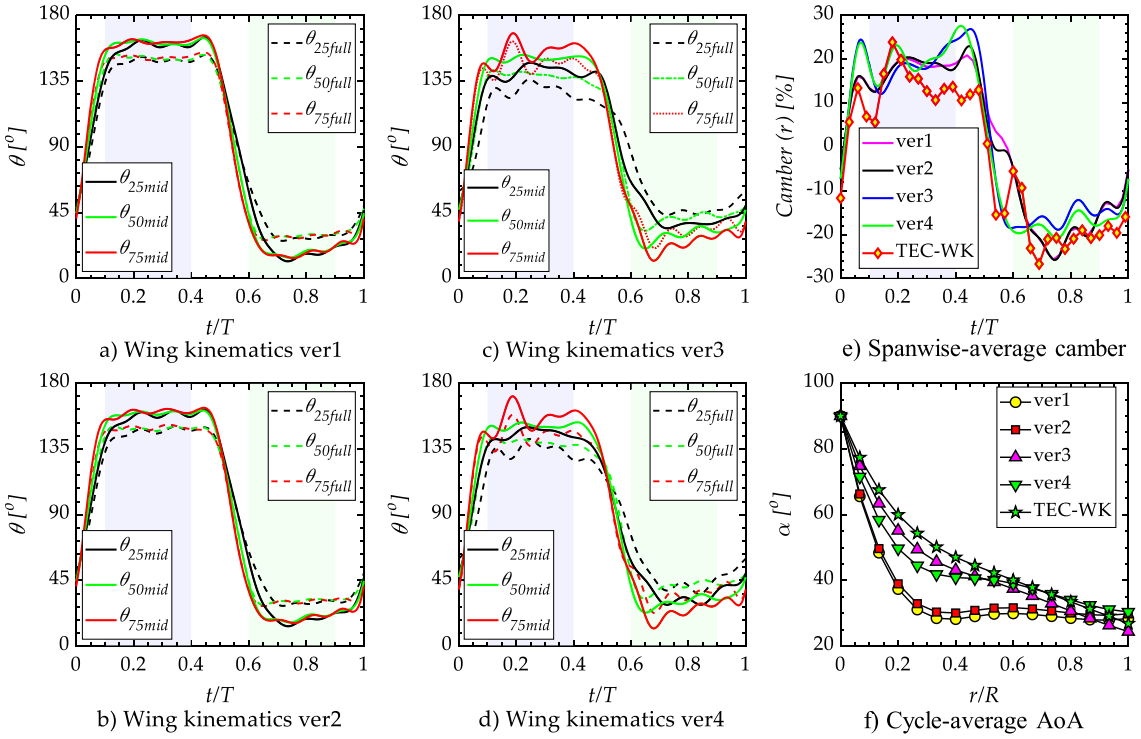

Fig. 5. Comparison of wing kinematics: a–d) Four versions of the modified wing kinematics at the three locations of (0.25, 0.5, and 0.75)R, e) spanwise-average camber, and f) cycle-average AoA of the five wing kinematics.

Table 1
Details of AoAs (α), the spanwise-average camber, and the CFD results of the five cases.

		Stroke(s)	AoA (α) [°]				Camber [%]	Results		
			0.25R	0.5R	0.75R	aver.		L [gf]	D [gf]	L/D
TEC-WK		*Downstroke*	55.4	43.4	34.7	39.9	14.5	9.4	8.5	1.1
		Upstroke	55.8	43.5	35.6	40.7	19.5	10.8	9.4	1.2
With camber but no twist	ver1	*Downstroke*	31.9	29.2	28.9	29.7	17.8	7.5	4.3	1.7
		Upstroke	32.6	29.8	29.0	29.9	19.3	8.6	4.8	1.8
	ver2	*Downstroke*	33.9	31.2	30.6	31.4	17.9	7.9	4.9	1.6
		Upstroke	34.2	31.4	30.5	31.5	19.3	8.8	5.4	1.6
With camber and twist	ver3	*Downstroke*	50.6	40.5	32.3	36.9	18.2	9.8	6.8	1.4
		Upstroke	50.6	40.4	32.4	37.0	16.5	9.9	7.3	1.4
	ver4	*Downstroke*	45.6	40.5	35.5	38.0	19.7	10.3	7.3	1.4
		Upstroke	45.4	40.4	35.3	37.8	18.1	10.5	8.0	1.3

leading-edge corrugation was found to have benefited the L/D [27]. Therefore, in this paper, several corrugation wings placed at the leading-edge were numerically tested. Fig. 6a shows sketches of the seven corrugated wing sections, divided into 3 groups: A, B, and C. Note that in (a), for simple presentation, the camber is removed. However, as in (b), the camber is passively placed in the actual flapping wing motion. These groups are classified based on their corrugation length (or wavelength). For example, the A-group represents the corrugated wing with a wavelength of 0.1c. Meanwhile, the B- and C-groups represent the wings with the wavelengths of 0.2c and 0.4c, respectively. The first two letters "LE" in the names stand for the wing corrugation placed near the leading edge after the flat wing area of 0.08c in all cases. Next, the first two digits denote the corrugation height as percentage of the local chord length, while the next two represent the proportion of the wavelength over the local wing chord. The last letter B (for bottom) denotes the B-type identified by the corrugation placed at the upper part of the chord, while the letter M (for middle) indicates the M-type standing for the corrugation implemented at the upper and lower parts of the chord.

3. Results

3.1. Effect of wing kinematics modulation

Table 2 shows the CFD simulation results for the TEC-WK and five modified wing kinematics, together with the cycle-average AoAs and spanwise-average cambers. For the first two wing kinematics ver1 and ver2 with chordwise camber but without spanwise twist, the cycle-average AoAs are about (30–32)°. The spanwise-average cambers of ver1 and ver2 are about 18.6%, which are slightly larger than that of the TEC-WK of about 17%. Ver1 shows reduction of the lift and drag for about (20.7 and 49.3)% respectively, resulting in a surge of the L/D for 57.5%, compared to those of the TEC-WK. Meanwhile, the increase in the L/D for ver2 is about 44.3%. On the other hand, ver3 and ver4 with chordwise camber (Fig. 5e) and spanwise wing twist (Fig. 5f) show the satisfactory lift production of about 20 gf. The spanwise-average camber of ver3 is about 17.2%, while that of ver4 is approximate 18.9%. The lift and drag of ver3 are (3 and 21)%, respectively, lower than those of TEC-WK, while the L/D increases by 24%. Similarly, the wing kinematics ver4 increases the L/D by 20%.

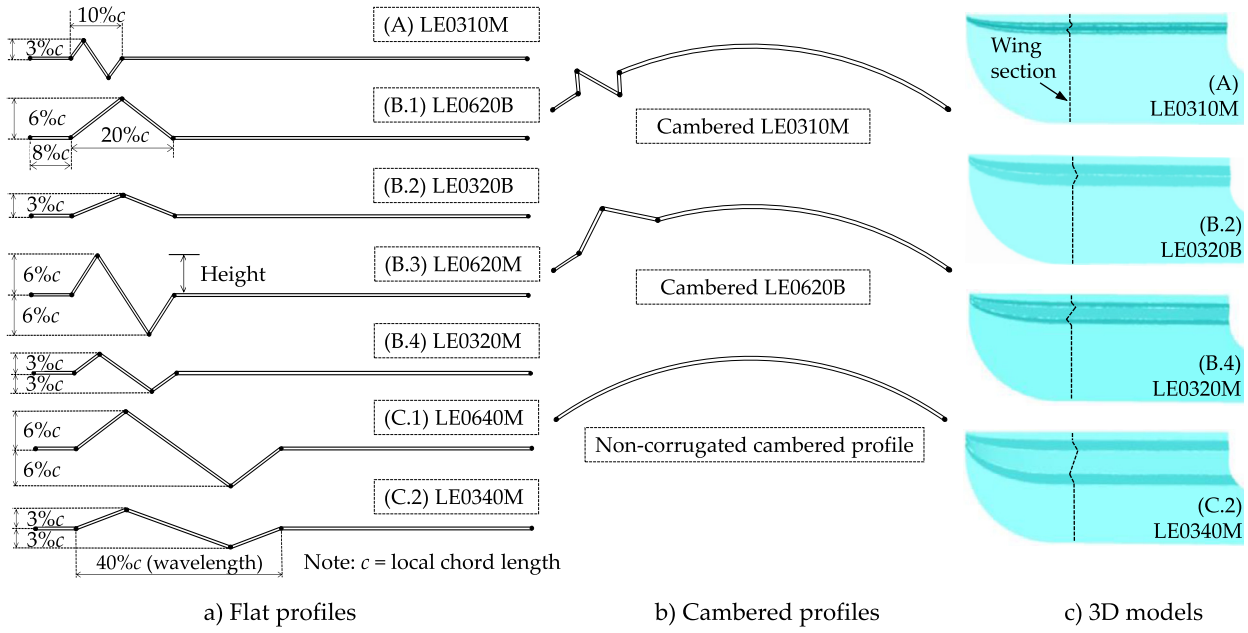

Fig. 6. Tested corrugated wings: a) Seven corrugated wing models divided into three groups: A, B, and C (flat configuration), b) cambered configuration of wings, c) four representatives of the M-type and B-type wings.

Table 2
Cycle-average AoAs and CFD results for the TEC-WK and modified wing kinematics over a flapping cycle.

Case(s)	Name	AoA [°]	Camber [%]	L [gf]	D [gf]	L/D
Reference	TEC-WK	40.3	17.0	20.3	17.95	1.13
Camber only	ver1	29.8	18.6	16.1 (−20.7%)	9.1 (−49.3%)	1.78 (+57.5%)
	ver2	31.4	18.6	16.8 (−17.2%)	10.3 (−42.6%)	1.63 (+44.3%)
Twist and camber	ver3	36.9	17.2	19.7 (−2.9%)	14.1 (−21.4%)	1.39 (+24.0%)
	ver4	37.9	18.9	20.7 (+2.0%)	15.3 (−14.8%)	1.35 (+19.5%)
Twist only	ver3*	36.9	0.0	16.9 (−16.7%)	13.5 (−24.8%)	1.25 (+10.6%)

Even though ver1 and ver2 provided high L/D, their generated lifts are not large enough to compensate for the weight. Moreover, it is challenging to develop a wing with constant AoA along the wingspan, while still forming a chordwise camber shape. Therefore, ver3 is chosen for further investigation, as presented in the next sections. In addition, to investigate the effect of chordwise camber, we removed the camber in the wing kinematics ver3, and estimated the lift and drag generations, as shown in Table 2 for ver3* with the twist-only case. The results in Table 2 show that the camber (of the ver3 case) increases the lift by 16.6% (19.7 gf and 16.9 gf) and the drag by 4.4%, resulting in 11.2% improvement of the L/D, which results are compared to those of the twist-only case ver3*. Since the lift produced by the modified wing kinematic ver3 is close to that by TEC-WK, while the drag is significantly decreased, the mechanism for force production is investigated and compared to that of TEC-WK.

Fig. 7 indicates the vortex structures over a flapping cycle for (a) the measured wing kinematics (TEC-WK), and (b) the modified wing kinematics ver3. The deformed wing shape and vortical structures of both cases are basically similar. However, the formed vorticities at t/T = (0.2 and 0.6) of both cases are quite different. At $t/T = 0.2$, for the modified wing kinematics ver3 (Fig. 7b), larger LEV is mainly formed and concentrated at the outboard wing, compared to those formed by the measured wing kinematics (Fig. 7a). As elsewhere reported [5,56], lower pressure due to the larger LEV enhances the lift generation. In contrast, at $t/T = 0.6$, the wing kinematics ver3 produces smaller LEVs at the outboard wing (Fig. 7b), compared to those by the measured wing kinematics (Fig. 7a). Figs. 8 show the lift (a1, a2) and drag (b1, b2) at point 1 ($t/T = 0.21$) and point 2 ($t/T = 0.54$) at $r/R = 0.88$ for both wing kinematics. At point 1, the modified wing kinematics ver3 increases the lift by 49.6%, but at point 2, it reduces it by about 69.8% (see Figs. 8a1 and a2), which values are compared to those of the reference TEC-WK. As a result, at point 1, the drag, which is here defined as the horizontal component of the resultant force, also increases by about 38.1%, and at point 2, reduces by 71.0% (see Figs. 8b1 and b2).

In summary, these plots show that when compared to that of TEC-WK, the cycle-average lift created by the wing kinematics of ver3 is almost unchanged, while its cycle-average drag is relatively lower, which satisfies the aerodynamic efficiency enhancement. As a result, the modified wing kinematics ver3 is chosen to further investigate the effect of the wing corrugation and clap-and-fling mechanism on the aerodynamic efficiency, which effect is presented in the following subsections.

3.2. Effect of the wing corrugation

Table 3 presents the cycle-average lift, drag, and aerodynamic efficiency of the seven corrugated wings tested with wing kinematic ver3, which are compared to those of the non-corrugated wing. The cycle-average lift generated by LE0620M and LE0640M is reduced by about (1.6 and 2.4)%, respectively. Meanwhile, the amount of change in the lift of the others is almost insignificant. On the other hand, except for LE0310M and LE0640M showing a decrease of about (1.0 and 1.8)% in drag, respectively, the other

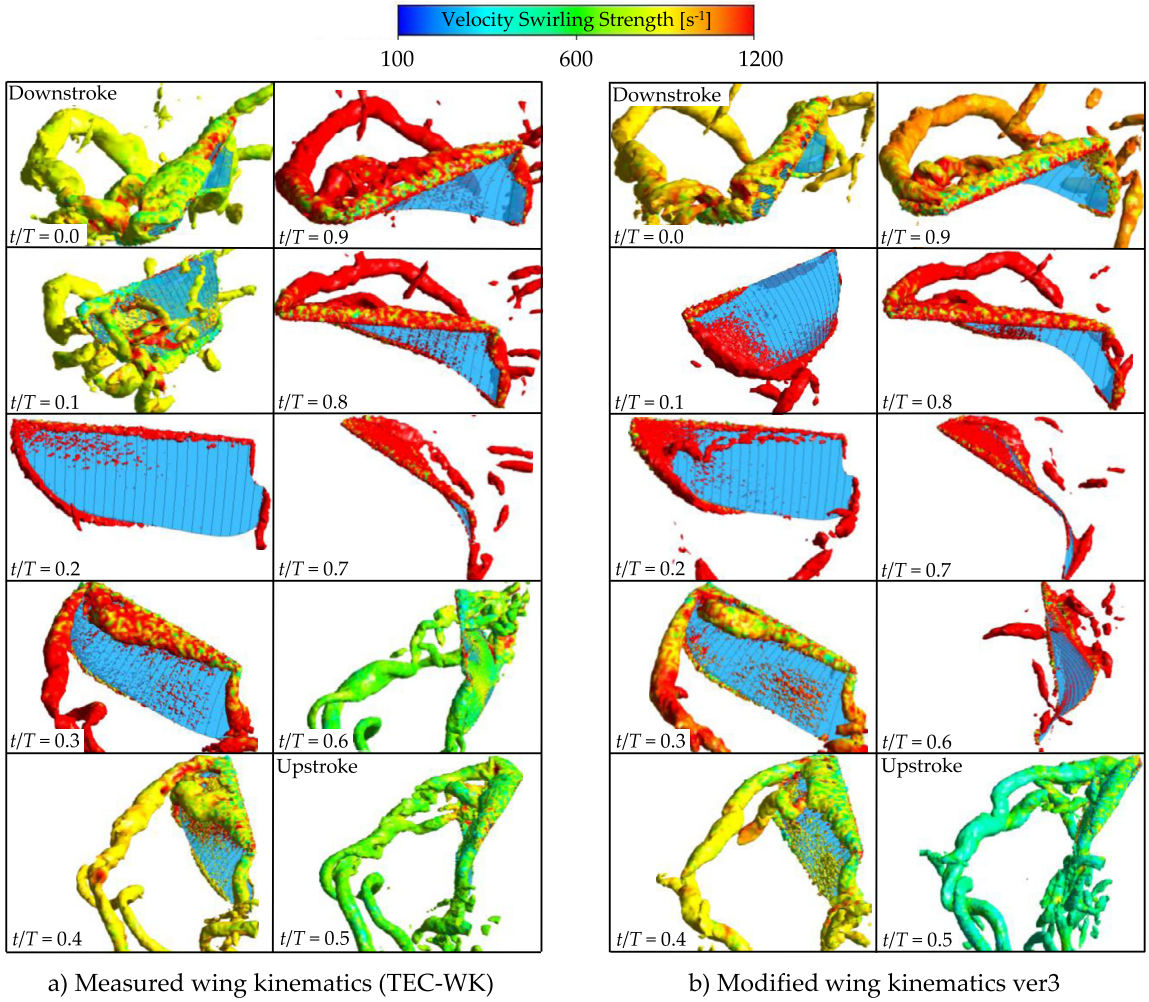

a) Measured wing kinematics (TEC-WK) b) Modified wing kinematics ver3

Fig. 7. Vortex structures visualized using the Q-criterion over a flapping wing cycle: a) for the measured reference wing kinematics TEC-WK, and b) for the modified wing kinematics ver3.

wings increase the cycle-average drag. Hence among the tested corrugated wings, LE0310M demonstrates the best cycle-average L/D, accounting for a 1.0% increase. To be clear, Fig. 9 compares the spanwise changes in L, D, and L/D of the seven wings with those of the non-corrugated wing. There are five regions along the wingspan that show the five remarkable tendencies in ΔL, ΔD, and $\Delta(L/D)$. From the wing root to $0.1R$, significant changes can be observed in the three quantities (Figs. 9a–c), while the variations of L and D are quite a bit smaller in $(0.1–0.5)R$ (Figs. 9a and b). Then, the changes seem evident in the outboard wing $(0.5–0.75)R$ and $(0.75–0.9)R$, especially in the wing tip $(0.9–1.0)R$. LE0310M shows similarity of lift with the non-corrugated wing from $0.1R$ to the wing tip (Fig. 9a), while its drag reduces, especially at $(0.1–0.5)R$ (Fig. 9b). Therefore, the L/D of LE0310M is relatively higher than those of the other wings (Fig. 9c).

In Fig. 9, the lift enhancement in the inboard wing can be seen to be up to 10%. But the overall lift enhancement in the whole wing is limited to a few percentage points (see Table 3). The reason is that the inboard wing's contribution to the lift generation is smaller than that of the outboard wing. This result is consistent with those from other cases [31,57], which claimed that when the geometric AoAs were less than 40°, there was almost no contribution of a wing corrugation to lift enhancement. For clearer analysis, Fig. 10 presents the changes in L, D, and L/D of the seven wings compared to those of the non-corrugated wing at the five wing locations. The reference results of L and L/D for the non-corrugated wing are located at the origin of the plots. Meanwhile, the reference D is represented by zero in the color bars of each plot. For example, the color changes of the symbols, compared to those at zero (non-corrugated wing), imply that the drag in each of these cases is less than or higher than the reference D. Fig. 10a shows the results at the locations from the wing root $(0R)$ to $0.1R$. In this range, LE0620M increases the L/D by about 8%, and the lift by 1.5%, but reduces the drag by 5.0%. Meanwhile, LE0310M yields increase of nearly (7, 3, and 5)% in the L, D, and L/D, respectively. In the range of wing locations in $(0.1 – 0.5)R$ (Fig. 10b), since the lift slightly increases by 1.0% and the drag decreases by about 2.0%, LE0310M demonstrates the highest L/D, accounting for about 3.5% higher than that of the non-corrugated case. Thus, LE0310M is suggested for the area from the root to $0.5R$.

At the wing location of $(0.5 – 0.75)R$ (Fig. 10c), the M-type wings with the corrugation height of 6% of c perform poorer than the other wings. For example, the lift produced by LE0620M is the lowest, while the L/D of LE0640M is the worst. In contrast, the B-type wings produce larger lifts and higher L/Ds. Fig. 10c shows that LE0620B outperforms the others. As a result, LE0620B is suggested for the locations in $(0.5 – 0.75)R$. At the outboard area, in $(0.75 – 0.9)R$ (Fig. 10d), as the height and length of corrugation become larger, the results of M-type wings tend to move to the left of the plot (i.e., becoming worse). This implies that among the analyzed M-type wings, LE0310M produces the best performance. However, LE0320B produces the highest lift. In order to meet the

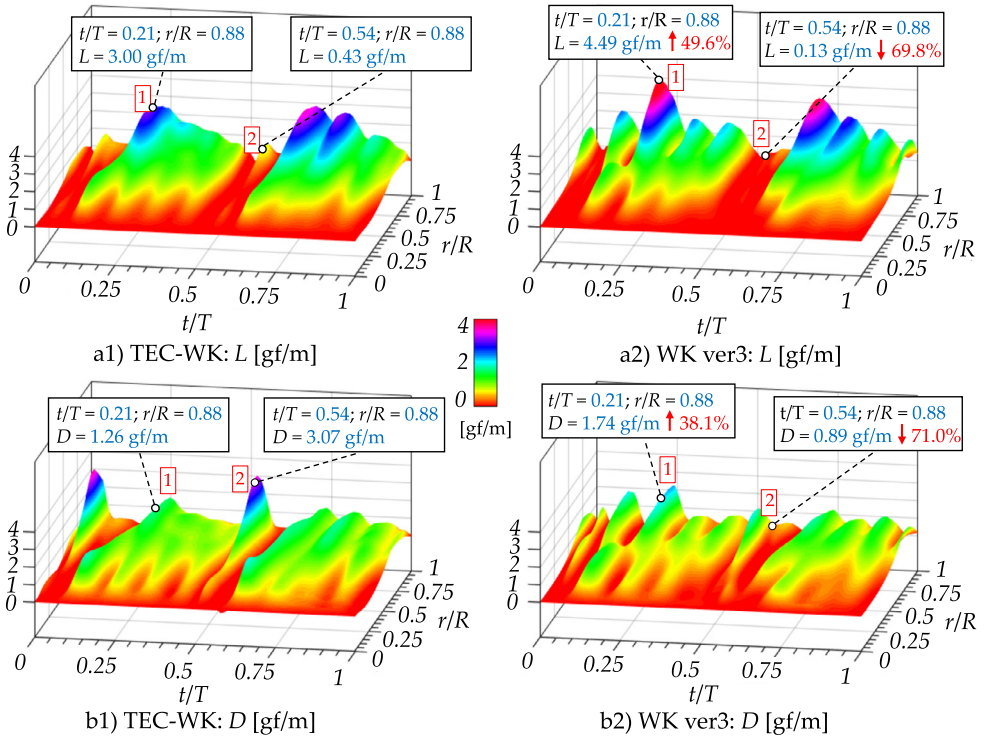

Fig. 8. Results of L (a1, a2) and D (b1, b2) for the measured wing kinematics (TEC-WK) and modified wing kinematics (WK ver3).

Table 3
Average L, D, and L/D of the seven corrugated wings, compared to those of the non-corrugated wing (Non-cor.).

	Stroke(s)	Non-cor.	LE0310M	LE0620B	LE0320B	LE0620M	LE0320M	LE0640M	LE0340M
L [gf]	Downstroke	9.76	9.74 (−0.2%)	9.94 (+1.8%)	9.86 (+1.0%)	9.65 (−1.1%)	9.80 (+0.4%)	9.58 (−1.8%)	9.74 (−0.2%)
	Upstroke	9.93	9.93 (+0.0%)	9.74 (−1.9%)	9.95 (+0.2%)	9.73 (−2.0%)	9.93 (+0.0%)	9.64 (−2.9%)	9.93 (+0.0%)
	Total	19.69	19.67 (−0.1%)	19.68 (−0.1%)	19.81 (+0.6%)	19.38 (−1.6%)	19.73 (+0.2%)	19.21 (−2.4%)	19.67 (−0.1%)
D [gf]	Downstroke	6.79	6.67 (−1.8%)	6.84 (+0.7%)	6.74 (−0.7%)	6.64 (−2.2%)	6.77 (−0.3%)	6.75 (−0.6%)	6.74 (−0.8%)
	Upstroke	7.33	7.30 (−0.4%)	7.41 (+1.1%)	7.47 (+1.9%)	7.22 (−1.5%)	7.34 (+0.1%)	7.58 (+3.4%)	7.43 (+1.4%)
	Total	14.11	13.97 (−1.0%)	14.25 (+1.0%)	14.22 (+0.7%)	13.86 (−1.8%)	14.11 (+0.0%)	14.34 (+1.5%)	14.17 (+0.4%)
L/D [%]	Downstroke	1.44	1.46 (+1.4%)	1.45 (+0.7%)	1.46 (+1.4%)	1.45 (+0.7%)	1.45 (+0.7%)	1.42 (−1.4%)	1.45 (+0.4%)
	Upstroke	1.36	1.36 (+0.0%)	1.31 (−3.7%)	1.33 (−2.3%)	1.35 (−0.7%)	1.35 (−0.7%)	1.27 (−6.6%)	1.34 (−1.8%)
	Total	1.39	1.41 (+1.0%)	1.38 (−1.0%)	1.39 (+0.0%)	1.40 (+0.2%)	1.40 (+0.2%)	1.34 (−3.9%)	1.39 (−0.1%)

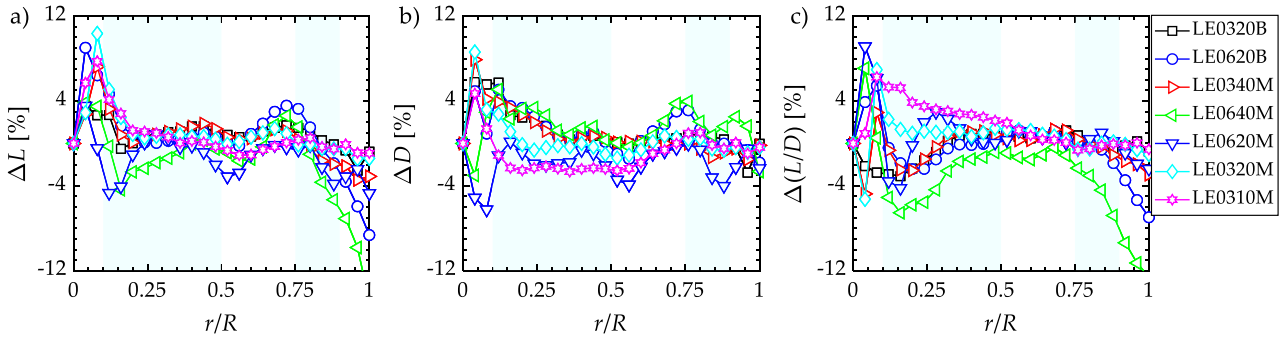

Fig. 9. Changes in L, D, and L/D of the seven corrugated wings, compared to that of the non-corrugated wing.

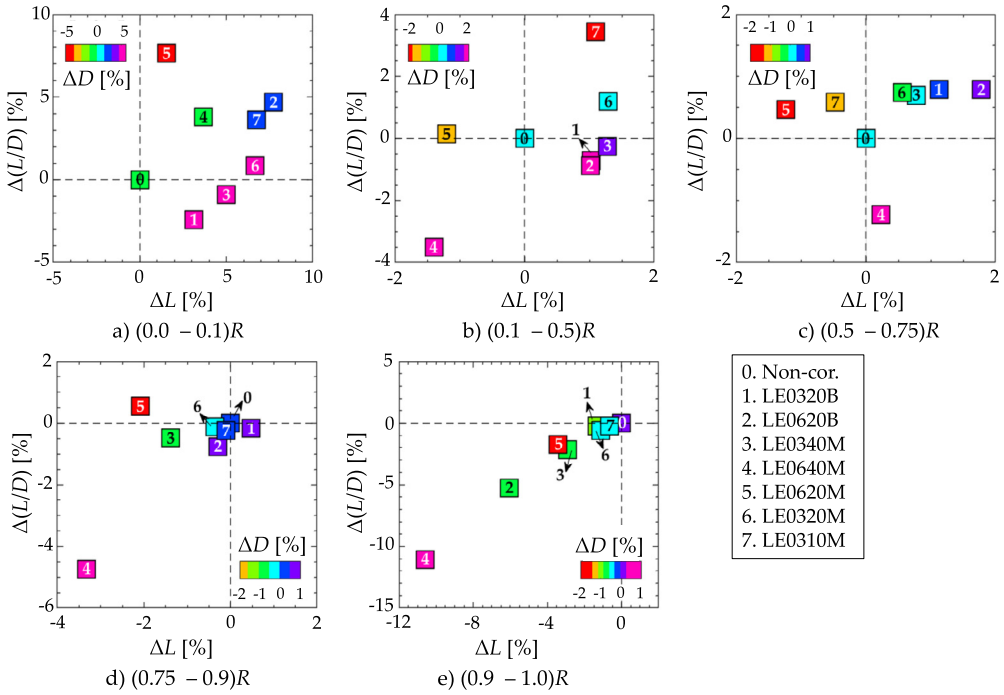

Fig. 10. Changes in L, D, and L/D of the seven corrugated wings compared to that of the non-corrugated wing at a) (0.0 – 0.1)R, b) (0.1 – 0.5)R, c) (0.5 – 0.75)R, d) (0.75 – 0.9)R, and e) (0.9 – 1.0)R.

lift requirement, LE0320B is recommended in the region (0.75 – 0.9)R. From 0.9R to the tip (Fig. 10e), none of the cases improve the L/D. Therefore, in this region, the non-corrugated wing is the best. In summary, the seven tested corrugated wings show different characteristics at each spanwise location. More specifically, for the wing location from the root to 0.5R, LE0310M is proposed. For (0.50 – 0.75)R, LE0620B outperforms the other wings. For the spanwise position in (0.75 – 0.9)R, the B-type LE0320B is selected, because it yields a higher lift than the others; while at the tip, the non-corrugated smooth wing is suggested.

Overall, from the wing root to 0.5R, the LE0310M improves the aerodynamic efficiency by about 5%, compared to that of the non-corrugated wing for the range of high AoAs from (50 to 80)°. However, when the AoAs become lower in the outboard wing (Fig. 5f), the aerodynamic efficiency of each of the corrugated wings reduces, especially from 0.75R to the wingtip. A similar tendency was found in the analysis of 2D flapping wings, as reported in [27]. Elsewhere [31], the aerodynamic performances between the corrugated wing of the dragonfly and the flat plate at the Re number range (500 to 10,000) were almost similar for small AoA of less than 10°. Kim et al. [57] showed that the effects of corrugated profiles based on the dragonfly wing section at Re numbers of 150, 1,400, and 10,000 were insignificant at AoAs up to 40°. Therefore, in this paper, we suggested a wing model employing different corrugated wings along the spanwise direction, which was named $N2$ wing, and investigated its aerodynamic performance.

Fig. 11a shows the non-corrugated wing configuration, and Fig. 11b displays the $N2$ wing with the corrugations implemented along the wingspan. The M-type corrugation is applied from the root to 0.5R, while the B-type wings are employed for (0.5 – 0.9)R. Fig. 11c compares the changes in L, D, and L/D of the $N2$ wing, and those of the non-corrugated wing. The results indicate that the cycle-average L/D increases for (0.0 – 0.1)R by 2.9%, for (0.1 – 0.5)R by 5.2%, and for the outer wing, decreases gradually. More clearly, Table 4 illustrates the cycle-average L, D, and L/D of the $N2$ wing for the entire wing length. The $N2$ wing produces almost the same lift, while over one cycle, the drag drops by about

Table 4
Average lift, drag, and aerodynamic efficiency of the non-corrugated and $N2$ wing configurations.

		Downstroke	Upstroke	Total
Non-cor.	L	9.76	9.93	19.70
	D	6.79	7.33	14.12
	L/D	1.44	1.36	1.39
$N2$	L	9.80 (+0.4%)	9.91 (−0.2%)	19.71 (+0.1%)
	D	6.77 (−0.4%)	7.09 (−3.2%)	13.86 (−1.9%)
	L/D	1.45 (+0.8%)	1.40 (+3.1%)	1.42 (+2.0%)

1.9%. Therefore, compared to that of the non-corrugated wing, the L/D of the $N2$ wing increases by over 2.0%. In more detail, Table 5 presents the results of the $N2$ wing at (0.15, 0.375, and 0.75)R. At 0.15R, the $N2$ wing shows a 6.0% increase of lift, while the drag reduces by 3%, which yields a surge of the L/D of about 9.3%. At 0.375R, the lift is the same, but its drag is lower by about 4.1%, producing an increase in L/D of about 3.5%. At 0.75R, since the wing shows a 1.5% increase in lift while the drag remains almost unchanged, the $N2$ wing shows a 1.8% increase in L/D. From this analysis, we may conclude that the $N2$ wing demonstrates about a 2% increase in the L/D. However, readers should note that this approach has limitations since flow interaction in the $N2$ wing was not considered.

3.3. Effect of the clap-and-fling

This section investigates the effect of the clap-and-fling on force generation for both cases of the TEC-WK and the modified wing kinematics ver3. In the KUBeetle design, the actual distance between the flapping axis and the symmetry plane is 8 mm (the distance between the two flapping axes = 16 mm) (Fig. 3b). For the case of no clap-and-fling effect, this distance is extended to 20 mm (the distance of two flapping axes = 40 mm), which is enough to remove the effect of clap-and-fling. Table 6 compares the results of L, D, and L/D of the four cases (a2) and (b1–3) to those of the reference case (a1). The study confirms that for both wing kinematics, the contribution of the clap-and-fling effect to lift

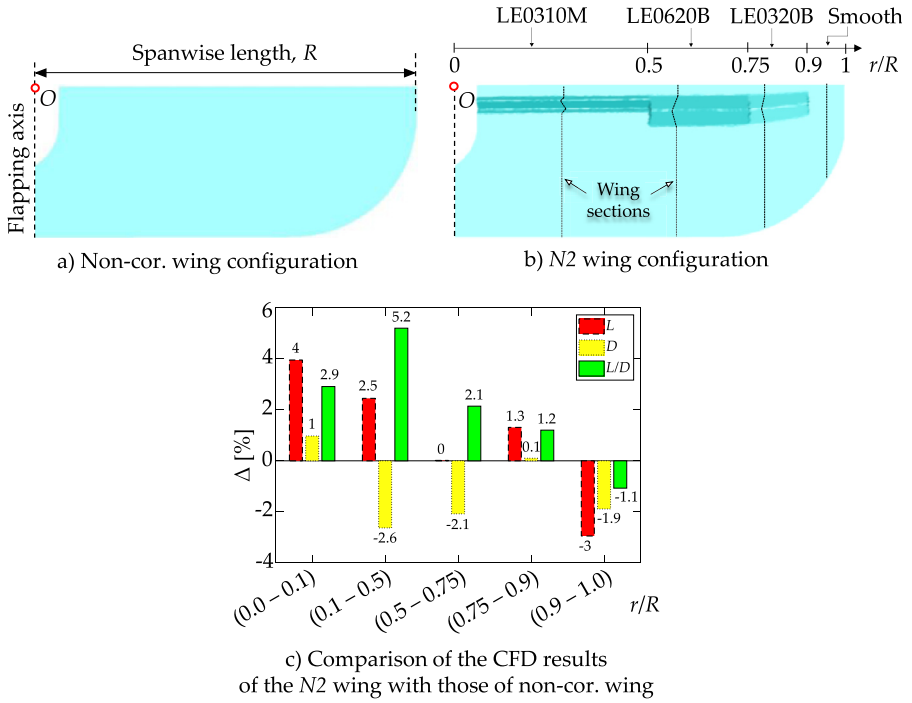

Fig. 11. Comparison of non-corrugated wing and *N*2 wing: a) Non-corrugated, b) *N*2 wing configurations, and c) CFD result comparison for both cases.

Table 5
Results of the *N*2 wing compared to the non-corrugated wing at (0.15, 0.375, and 0.75)*R*.

	0.15*R*	Non-cor.	*N*2	0.375*R*	Non-cor.	*N*2	0.75*R*	Non-cor.	*N*2
L [gf]	Downstroke	0.09	0.09 (+0.0%)	Downstroke	0.28	0.29 (+3.6%)	Downstroke	0.64	0.64 (+0.0%)
	Upstroke	0.09	0.10 (+11.0%)	Upstroke	0.29	0.28 (−3.5%)	Upstroke	0.66	0.67 (+1.5%)
	Total	0.18	0.19 (+6.0%)	Total	0.57	0.57 (+0.0%)	Total	1.30	1.32 (+1.5%)
D [gf]	Downstroke	0.17	0.18 (+6.0%)	Downstroke	0.24	0.24 (−0.0%)	Downstroke	0.34	0.34 (−0.0%)
	Upstroke	0.15	0.15 (−0.0%)	Upstroke	0.25	0.23 (−8.0%)	Upstroke	0.45	0.45 (−0.0%)
	Total	0.33	0.32 (−3.0%)	Total	0.49	0.47 (−4.1%)	Total	0.79	0.79 (−0.0%)
L/*D*	Downstroke	0.52	0.54 (+3.8%)	Downstroke	1.16	1.20 (+3.5%)	Downstroke	1.85	1.88 (+1.6%)
	Upstroke	0.57	0.65 (+14.0%)	Upstroke	1.15	1.20 (+4.4%)	Upstroke	1.49	1.51 (+1.4%)
	Total	0.54	0.59 (+9.3%)	Total	1.16	1.20 (+3.5%)	Total	1.64	1.67 (+1.8%)

Table 6
Effects of the wing kinematics modulation, wing corrugation, and clap-and-fling on *L*, *D*, and *L*/*D*.

L and *D* [gf]	a) TEC-WK						b) Modified wing kinematics ver3								
	a1) Non-cor. & C–F			a2) Non-cor. & N–C–F			b1) Non-cor. & C–F			b2) *N*2 & C–F			b3) *N*2 & N–C–F		
Stroke(s)	*L*	*D*	*L*/*D*	*L*	*D*	*L*/*D*	*L*	*D*	*L*/*D*	*L*	*D*	*L*/*D*	*L*	*D*	*L*/*D*
Downstroke	9.40	8.50	1.12	9.14 (−2.7%)	7.84 (−7.8%)	1.17 (+4.5%)	9.76 (+3.8%)	6.79 (−20.1%)	1.44 (+28.6%)	9.80 (+4.3%)	6.77 (−20.4%)	1.45 (+29.5%)	9.37 (−0.3%)	6.14 (−27.8%)	1.53 (+36.6%)
Upstroke	10.80	9.40	1.13	10.23 (−5.3%)	8.57 (−8.8%)	1.19 (+5.3%)	9.93 (−8.1%)	7.33 (−22.0%)	1.36 (+20.4%)	9.91 (−8.2%)	7.09 (−24.6%)	1.40 (+23.9%)	9.44 (−12.6%)	6.61 (−29.7%)	1.43 (+26.5%)
Total	20.30	17.95	1.13	19.37 (−4.6%)	16.42 (−8.5%)	1.18 (+4.4%)	19.70 (−3.0%)	14.12 (−21.3%)	1.39 (+23.0%)	19.71 (−2.9%)	13.86 (−22.8%)	1.42 (+25.7%)	18.80 (−7.4%)	12.74 (−29.0%)	1.48 (+30.9%)

"C–F" ≡ clap-and-fling; "N–C–F" ≡ non-clap-and-fling.

enhancement is about 4.8% (comparing the total lifts in a1 and a2, and those in b2 and b3 in Table 6); however, their produced drags also increase. In particular, in the TEC-WK, the clap-and-fling increases the cycle-average drag by 9.3% (comparing the total drags in a1 and a2), and in the modified wing kinematics ver3 by 8.8% (comparing the total drag in b2 and b3 for the *N*2 wing). Therefore, for both wing kinematics, the clap-and-fling cases tested show approximately (4.2 and 4.1)% lower in *L*/*D*, when compared to those in a1 and a2, and those in b2 and b3, respectively. Thus, the suggested *N*2 wing with the kinematic ver3 increases the cycle-average *L*/*D* by about (25.7 and 30.9)% for the clap-and-fling case and the non-clap-and-fling case, respectively, compared to the *L*/*D* of the TEC-WK (case a1 in Table 6). However, their lifts slightly decrease by about (2.9 and 7.4)%, respectively. In summary, even though the clap-and-fling contributes to the lift enhancement, it is inefficient for the KUBeetle robot. The result agrees with that in the study by Miller and Peskin on tiny insects at low *Re*, in which the clap-and-fling for the rigid wing increased the drag ten times, and for the flexible wing, five times [58].

4. Conclusions

This paper presented a CFD study on the aerodynamic efficiency of the KUBeetle that considered the effects of wing kinematics, corrugation structures, and the clap-and-fling mechanism. Based on the measured reference wing kinematics, four wing kinemat-

ics were investigated to find the proper one that would improve L/D, while maintaining similar lift. The results of the modified wing kinematics ver3 with camber and twist outperformed the other suggested cases, improving the aerodynamic efficiency by 24%, while producing enough lift to compensate for the weight. The study also confirmed that the chordwise camber improves both lift and L/D by about (16.7 and 10.6)%, respectively. Then, the effects of various corrugations were investigated with wing kinematics ver3. From the results of lift and L/D, we proposed a corrugated $N2$ wing with different corrugations distributed along the wingspan. Although the $N2$ wing slightly increases the L/D by about 2%, this research contributes to the idea in designing a wing for FW-MAVs of unifying different corrugation structures along the spanwise direction. Finally, we examined the contribution of the clap-and-fling on the force generation at the stroke reversals. The results revealed that the clap-and-fling contributes to both lift and drag improvement, by about (5 and 9)%, respectively, resulting in about 4% reduction of L/D for both wing kinematics. Therefore, the clap-and-fling benefits lift, but reduces aerodynamic efficiency. In conclusion, if the clap-and-fling effect is eliminated, the corrugated $N2$ wing using the wing kinematics ver3 may increase the aerodynamic efficiency of the KUBeetle robot by 31%. The question then arises of how can we reproduce the suggested wing kinematics? Since the wing of the KUBeetle is made of a thin plastic film reinforced with thin carbon/epoxy strips, the passive wing deformation differs, depending on the pattern of the strip. Therefore, we can tailor the strip pattern to passively reproduce the suggested wing kinematics, especially ver3 and ver4, which are more physically feasible. In addition, the trailing-edge position at the wing root can be either passively or actively shifted during flapping strokes to modify the wing rotation characteristics. We will report the relevant research progress in the near future.

Declaration of competing interest

The authors declare that they have no known competing financial interests or personal relationships that could have appeared to influence the work reported in this paper.

Acknowledgements

This research was supported by a National Research Foundation of Korea (NRF) grant, funded by the Korean government (MSIT) (NRF-2018R1A4A1024191).

References

[1] D.E. Alexander, Nature's Flyers: Birds, Insects, and the Biomechanics of Flight, The Johns Hopkins University Press, Baltimore, 2002 (Chapter 4).
[2] M. Sun, Insect flight dynamics: stability and control, Rev. Mod. Phys. 86 (2) (2014) 615.
[3] H.V. Phan, H.C. Park, Insect-inspired, tailless, hover-capable flapping-wing robots: recent progress, challenges, and future directions, Prog. Aerosp. Sci. 111 (2019) 100573.
[4] L. Chen, J. Wu, B. Cheng, Leading-edge vortex formation and transient lift generation on a revolving wing at low Reynolds number, Aerosp. Sci. Technol. 97 (2020) 105589.
[5] W. Shyy, H. Liu, Flapping wings and aerodynamic lift: the role of leading-edge vortices, AIAA J. 45 (12) (2007) 2817–2819.
[6] J.M. Birch, M.H. Dickinson, The influence of wing–wake interactions on the production of aerodynamic forces in flapping flight, J. Exp. Biol. 206 (13) (2003) 2257–2272.
[7] K.B. Lua, T.T. Lim, K.S. Yeo, Effect of wing–wake interaction on aerodynamic force generation on a 2D flapping wing, Exp. Fluids 51 (1) (2011) 177–195.
[8] J.S. Han, J.W. Chang, J.K. Kim, J.H. Han, Role of trailing-edge vortices on the hawkmothlike flapping wing, J. Aircr. 52 (4) (2015) 1256–1266.
[9] M. Dickinson, The effects of wing rotation on unsteady aerodynamic performance at low Reynolds numbers, J. Exp. Biol. 192 (1) (1994) 179–206.
[10] S.P. Sane, M.H. Dickinson, The aerodynamic effects of wing rotation and a revised quasi-steady model of flapping flight, J. Exp. Biol. 205 (8) (2002) 1087–1096.
[11] T. Weis-Fogh, Quick estimates of flight fitness in hovering animals, including novel mechanisms for lift production, J. Exp. Biol. 59 (1973) 169–230.
[12] M. Lighthill, On the Weis-Fogh mechanism of lift generation, J. Fluid Mech. 60 (1) (1973) 1–17.
[13] S. Sane, The aerodynamics of insect flight, J. Exp. Biol. 206 (23) (2003) 4191–4208.
[14] C. Ellington, The novel aerodynamics of insect flight: applications to micro-air vehicles, J. Exp. Biol. 202 (23) (1999) 3439–3448.
[15] J. Marden, Maximum lift production during takeoff in flying animals, J. Exp. Biol. 130 (1) (1987) 235–258.
[16] H.V. Phan, T.K.L. Au, H.C. Park, Clap-and-fling mechanism in a hovering insect-like two-winged flapping-wing micro air vehicle, R. Soc. Open Sci. 3 (12) (2016) 160746.
[17] A.T. Nguyen, J.H. Han, Wing flexibility effects on the flight performance of an insect-like flapping-wing micro-air vehicle, Aerosp. Sci. Technol. 79 (2018) 468–481.
[18] A.M. Mountcastle, S.A. Combes, Wing flexibility enhances load-lifting capacity in bumblebees, Proc. R. Soc. B, Biol. Sci. 280 (2013) 20130531.
[19] M. Okamoto, K. Yasuda, A. Azuma, Aerodynamic characteristics of the wings and body of a dragonfly, J. Exp. Biol. 199 (2) (1996) 281–294.
[20] S. Deng, J. Wang, H. Liu, Experimental study of a bio-inspired flapping wing MAV by means of force and PIV measurements, Aerosp. Sci. Technol. 94 (2019) 105382.
[21] Q.T. Truong, H.V. Phan, H.C. Park, J.H. Ko, Effect of wing twisting on aerodynamic performance of flapping wing system, AIAA J. 51 (7) (2013) 1612–1620.
[22] S. Chen, H. Li, S. Guo, M. Tong, B. Ji, Unsteady aerodynamic model of flexible flapping wing, Aerosp. Sci. Technol. 80 (2018) 354–367.
[23] S.P. Sane, M.H. Dickinson, The control of flight force by a flapping wing: lift and drag production, J. Exp. Biol. 204 (15) (2001) 2607–2626.
[24] H.V. Phan, Q.T. Truong, H.C. Park, An experimental comparative study of the efficiency of twisted and flat flapping wings during hovering flight, Bioinspir. Biomim. 12 (3) (2017) 036009.
[25] A. Gehrke, K. Mulleners, Phenomenology and scaling of optimal flapping wing kinematics, Bioinspir. Biomim. 16 (2) (2021) 026016.
[26] C.J.C. Rees, Form and function in corrugated insect wings, Nature 256 (5514) (1975) 200–203.
[27] T.T. Dao, T.K.L. Au, S.H. Park, H.C. Park, Effect of wing corrugation on the aerodynamic efficiency of two-dimensional flapping wings, Appl. Sci. 10 (20) (2020) 7375.
[28] A.B. Kesel, Aerodynamic characteristics of dragonfly wing sections compared with technical aerofoils, J. Exp. Biol. 203 (20) (2000) 3125–3135.
[29] T.K.L. Au, H.V. Phan, S.H. Park, H.C. Park, Effect of corrugation on the aerodynamic performance of three-dimensional flapping wings, Aerosp. Sci. Technol. 105 (2020) 106041.
[30] X.G. Meng, L. Xu, M. Sun, Aerodynamic effects of corrugation in flapping insect wings in hovering flight, J. Exp. Biol. 214 (3) (2011) 432–444.
[31] A. Vargas, R. Mittal, H. Dong, A computational study of the aerodynamic performance of a dragonfly wing section in gliding flight, Bioinspir. Biomim. 3 (2) (2008) 026004.
[32] M. Keennon, K. Klingebiel, H. Won, Development of the nano hummingbird: a tailless flapping wing micro air vehicle, in: 50th AIAA Aerospace Sciences Meeting, 2012, p. 588.
[33] H.V. Phan, T.S. Kang, H.C. Park, Design and stable flight of a 21 g insect-like tailless flapping wing micro air vehicle with angular rates feedback control, Bioinspir. Biomim. 12 (3) (2017) 036006.
[34] A. Roshanbin, H. Altartouri, M. Karásek, A. Preumont, COLIBRI: a hovering flapping twin-wing robot, Int. J. Micro Air Veh. 9 (4) (2017) 270–282.
[35] K.Y. Ma, P. Chirarattananon, S.B. Fuller, R.J. Wood, Controlled flight of a biologically inspired, insect-scale robot, Science 340 (6132) (2013) 603–607.
[36] M. Karásek, F.T. Muijres, C. De Wagter, B.D. Remes, G.C. de Croon, A tailless aerial robotic flapper reveals that flies use torque coupling in rapid banked turns, Science 361 (6407) (2018) 1089–1094.
[37] Q.V. Nguyen, L.C. Woei, Development and flight performance of a biologically-inspired tailless flapping-wing micro air vehicle with wing stroke plane modulation, Bioinspir. Biomim. 14 (1) (2018) 016015.
[38] Z. Tu, F. Fei, X. Deng, Untethered flight of an at-scale dual-motor hummingbird robot with bio-inspired decoupled wings, IEEE Robot. Autom. Lett. 5 (3) (2020) 4194–4201.
[39] G. Du, M. Sun, Effects of wing deformation on aerodynamic forces in hovering hoverflies, J. Exp. Biol. 213 (13) (2010) 2273–2283.
[40] L. Bennett, Clap and fling aerodynamics-an experimental evaluation, J. Exp. Biol. 69 (1) (1977) 261–272.
[41] S. Mao, Y.U. Xin, Flows around two airfoils performing fling and subsequent translation and translation and subsequent clap, Acta Mech. Sin. 19 (2) (2003) 103–117.
[42] F-O. Lehmann, S.P. Sane, M.H. Dickinson, The aerodynamic effects of wing–wing interaction in flapping insect wings, J. Exp. Biol. 208 (16) (2005) 3075–3092.
[43] Q.V. Nguyen, W.L. Chan, M. Debiasi, Design, fabrication, and performance test of a hovering-based flapping-wing micro air vehicle capable of sustained and controlled flight, in: International Micro Air Vehicle Conference, Delft, the Netherlands, Delft University of Technology, 2014.

[44] G.C.H.E. De Croon, K.M.E. De Clercq, R. Ruijsink, B. Remes, C. De Wagter, Design, aerodynamics, and vision-based control of the DelFly, Int. J. Micro Air Veh. 1 (2) (2009) 71–97.
[45] P. Zdunich, D. Bilyk, M. MacMaster, D. Loewen, J. DeLaurier, R. Kornbluh, D. Holeman, Development and testing of the mentor flapping-wing micro air vehicle, J. Aircr. 44 (5) (2007) 1701–1711.
[46] H.V. Phan, S. Aurecianus, T.K.L. Au, T. Kang, H.C. Park, Towards the long-endurance flight of an insect-inspired, tailless, two-winged, flapping-wing flying robot, IEEE Robot. Autom. Lett. 5 (4) (2020) 5059–5066.
[47] H.V. Phan, H.C. Park, Design and evaluation of a deformable wing configuration for economical hovering flight of an insect-like tailless flying robot, Bioinspir. Biomim. 13 (3) (2018) 036009.
[48] H.V. Phan, H.C. Park, Mechanisms of collision recovery in flying beetles and flapping-wing robots, Science 370 (6521) (2020) 1214–1219.
[49] T.K.L. Au, H.V. Phan, H.C. Park, Comparison of aerodynamic forces and moments calculated by three-dimensional unsteady blade element theory and computational fluid dynamics, J. Bionics Eng. 14 (4) (2017) 746–758.
[50] T.K.L. Au, H.V. Phan, H.C. Park, Longitudinal flight dynamic analysis on vertical takeoff of a tailless flapping-wing micro air vehicle, J. Bionics Eng. 15 (2) (2018) 283–297.
[51] T.K.L. Au, H.C. Park, Influence of center of gravity location on flight dynamic stability in a hovering tailless FW-MAV: longitudinal motion, J. Bionics Eng. 16 (1) (2019) 130–144.
[52] T.L. Hedrick, Software techniques for two- and three-dimensional kinematic measurements of biological and biomimetic systems, Bioinspir. Biomim. 3 (3) (2008) 034001.
[53] H. Blasius, Grenzschichten in Flüssigkeiten mit kleiner Reibung, Z. Math. Phys. 56 (1908) 1–37.
[54] Y. Lian, W. Shyy, Aerodynamics of low Reynolds number plunging airfoil under gusty environment, in: 45th AIAA Aerospace Sciences Meeting and Exhibit, 2007, p. 71.
[55] J. Young, J.C. Lai, C. Germain, Simulation and parameter variation of flapping-wing motion based on dragonfly hovering, AIAA J. 46 (4) (2008) 918–924.
[56] C.P. Ellington, C. Van Den Berg, A.P. Willmott, A.L. Thomas, Leading-edge vortices in insect flight, Nature 384 (6610) (1996) 626–630.
[57] W.K. Kim, J.H. Ko, H.C. Park, D. Byun, Effects of corrugation of the dragonfly wing on gliding performance, J. Theor. Biol. 260 (4) (2009) 523–530.
[58] L.A. Miller, C.S. Peskin, Flexible clap and fling in tiny insect flight, J. Exp. Biol. 212 (19) (2009) 3076–3090.